ELSEVIER

Contents lists available at ScienceDirect

### Additive Manufacturing

journal homepage: www.elsevier.com/locate/addma



## Experimentally validated predictions of thermal history and microhardness in laser-deposited Inconel 718 on carbon steel



Sarah J. Wolff<sup>a,1</sup>, Zhengtao Gan<sup>a,1</sup>, Stephen Lin<sup>a</sup>, Jennifer L. Bennett<sup>a,b</sup>, Wentao Yan<sup>a</sup>, Gregory Hyatt<sup>b</sup>, Kornel F. Ehmann<sup>a</sup>, Gregory J. Wagner<sup>a</sup>, Wing Kam Liu<sup>a,\*</sup>, Jian Cao<sup>a</sup>

- <sup>a</sup> Mechanical Engineering, Northwestern University, Evanston, IL 60208, USA
- b DMG MORI, Hoffman Estates, IL 60192, USA

#### ARTICLE INFO

# Keywords: Additive manufacturing Thermal-CFD modeling Cooling rate Microhardness Inconel 718

#### ABSTRACT

Process – property relationships in additive manufacturing (AM) play critical roles in process control and rapid certification. In laser-based directed energy deposition, powder mass flow into the melt pool influences the cooling behavior and properties of a built part. This study develops predictive computational models that provide the microhardness of AM components processed with miscible dissimilar alloys, and then investigates the influence of varying process parameters on properties in experiments and modeling. Experimentally-determined clad dilution and microhardness results of Ni-based superalloy Inconel 718 clads deposited onto 1045 carbon steel substrates are compared to the values from a computational thermo-fluid dynamics (CtFD) model. The numerical model considers the fluidic mechanisms of molten metal during powder deposition and the resulting transient melt pool geometry changes. The model also handles the change in thermo-physical properties caused by the composition mixture between the powder and substrate materials in the melt pool. Based on the computed temperature and velocity distributions in the melt pool, cooling rate, dilution of the melt pool and microhardenss are evaluated. The capability to predict thermal histories in such models is calibrated and validated with experimental thermal imaging and microstructures of additive manufactured clads. In addition, the roles of cooling rate and alloy composition on the microhardness are examined. The results show that variation in microhardness is dominated by composition mixture between the powder and substrate materials, rather than cooling behavior or dendrite arm spacing at liquid-solid interface in laser deposited Inconel 718 on AISI 1045 carbon steel.

#### 1. Introduction

Directed energy deposition (DED) is an additive manufacturing process and attractive tool to fabricate and repair high-strength certifiable materials for transportation and various industries. In DED, a laser beam melts the substrate, creating a melt pool into which metal powders are deposited [1,2]. The interaction of a laser with blown metallic powders in DED has advantages over traditional processes such as welding and casting, due to a small heat affected zone [3]. Ni-based alloys have been widely used as the deposited material to improve yield strength, ultimate tensile strength, wear and corrosion resistance at the surface of a product [4,5]. In particular, Inconel 718, or IN718, has numerous applications as turbine components due to its high temperature yield strength and corrosion resistance [6].

To assess the highly transient manufacturing process, a few models

have been developed. There are two major types of models: the thermal model and the thermo-fluid flow model. Gao et al. [7] developed a 3D thermal model using the finite element method (FEM) to calculate the thermal gradient and the solidification rate in the liquid–solid interface of an iron-based alloy mixed with titanium powders in laser cladding. Using a Fourier heat conduction model, the effects of preheating a 1030 carbon steel substrate on cooling of deposited FeTiC composite particles in laser cladding were investigated in a thermal model [8]. Microstructure analysis of Ti-C particles and microhardness testing were compared to the temperature distribution of the clad. However, neither fluid flow in the melt pool nor powder catchment efficiency were considered in these numerical models.

Several thermo-fluid flow models for the DED process have been developed. Qi et al. [9] built a three-dimensional thermal fluid model to calculate the temperature distribution and liquid metal flow in the melt

<sup>\*</sup> Corresponding author.

E-mail addresses: w-liu@northwestern.edu (W.K. Liu), jcao@northwestern.edu (J. Cao).

<sup>&</sup>lt;sup>1</sup> These authors contributed equally to this work.

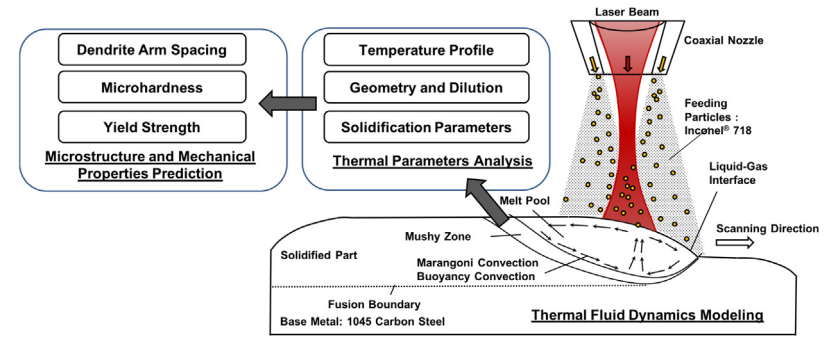


Fig. 1. Multi-physical phenomena, thermal parameters analysis and microhardness prediction in DED.

pool during the direct metal deposition (DMD) process of low-carbon steel powders. The trends in melt pool length, melt pool width, and clad height with increasing laser power were the same as those in experiments. He et al. [10] captured powder deposition of ANSI H13 tool steel powders onto a low-carbon steel substrate in DMD by using a computationally intensive approach, the Level-Set method, to capture the melt pool interface. Trends in clad dilution with increasing laser power and scanning speed were similar to those in experiments. Kumar et al. [11] derived and solved sets of dimensionless conservation equations to predict the melt pool dimensions, temperature distribution and cooling rates during the laser cladding of iron powders. They found that the influence of Marangoni-Benard convection dominates the simulation results. Shin's group [12] developed a series of models to investigate the transport phenomena in off-axis high power diode laser cladding of stellite powder. The experimental and predicted values of powder velocity during deposition, clad height, and clad width were compared. Gan et al. [13] proposed a physical-based model with Marangoni convection to predict the thermal distribution and solute transport in the melt pool during the direct laser deposition of cobalt-based powders onto a steel substrate. The temperature field results from their model provide solidification parameters such as thermal gradient, solidification rate, cooling rate, and morphology factor. These values were compared to the experimental clad profile and microstructures within the clad.

Thermal gradient (G) and solidification rate (R) have been proven to be two key parameters in predicting the solidified grain and dendrite structure, and, ultimately, the mechanical properties [14]. Tang et al. [15] used an analytical Rosenthal model to obtain the G-R relationship and developed a statistical model for dendrite arm spacing in selective laser melting of AlSi10Mg. Liu et al. [16] calculated cooling rate based on finite element method (FEM) to evaluate gradients in microstructure and mechanical properties, with greater hardness with finer dendrites. Acharya et al. [17,18] used a thermo-fluid model to predict the G-R relationship and evaluated dendrite arm spacing based on Hunt's model and Rappaz modification in laser additive manufacturing of single crystal alloy CMSX-4. Wang et al. [19] used a combined cellular-automation-finite difference model to evaluate the G-R relationship during solidification of nickel-based superalloys and the resulting dendritic structures and spacing. Nie et al. [20] used a combined finite element method and stochastic analysis model to evaluate the multi-scale evolution of microstructure during the solidification of laser-processed nickel-based superalloys. They found good agreement between experiments and the G-R relationship from simulations, concluding that lower cooling rates could result in the Laves phase, which is detrimental to mechanical properties. Keller et al. [21] also used combined modeling methods to investigate the solidification of nickel-based superalloys, including finite element methods to output melt pool characteristics, CALPHAD-based methods including DICTRA to evaluate microsegregation, and phase-field models for dendritic arm spacing. Debroy et al. [22,23] proposed an empirical model to predict dendrite arm spacing and microhardness based on cooling rate at liquidus

temperature during the powder bed processes of 316L stainless steel. The microhardness depends on secondary dendrite arm spacing in this work [22].

Microhardness of additively manufactured aluminum, nickel, titanium and iron based components has been summarized in a review [14]. However, most previous studies that used modeling to predict microhardness using G-R relationships only looked at a single material system. A few references have shown the capability of AM-processed functionally graded materials [24] and multi-materials [25], in which the powder and substrate are dissimilar materials. Choosing suitable dissimilar alloys for powder and substrates is critical for laser-based additive processing [13]. Understanding the process and predicting mechanical properties for AM processing of miscible dissimilar alloys systems remain a challenge.

In the current work, to understand the influence of both thermal history and composition dilution on the microhardness of the deposited track of IN718 clad onto a 1045 steel substrate, both experiments and numerical simulations are performed with varying process parameters. Thermal imaging and *ex-situ* material characterization are conducted. A thermo-fluid dynamics model is employed to simulate the temperature profile and melt pool flow. Based on the simulation results, the cooling and solidification rates between solidus and liquidus temperature of the moving melt pool are evaluated. This leads to a better understanding of the relationship between the temperature profile and experimentally measured micro-hardness. The overall schematic for this framework is seen in Fig. 1.

#### 2. Experimental methods

#### 2.1. Processing of IN718 single clads

A DMG MORI LaserTec 65 3D, a hybrid additive and subtractive five-axis machine, is used to build single clads. A 2500 W, 1020 nm, high-powered continuous wave laser melted deposit IN718 powders onto an AISI 1045 medium carbon steel substrate, as seen in Fig. 2a. The beam diameter at its focus is 3 mm. IN718 powders of  $50-150 \mu m$ in diameter are deposited into the melt pool. Shielding and carrier gas consist of argon with a flow rate of 7 L/min. The single line IN718 clads built in [26] to evaluate clad height are used in this study to evaluate dilution, microhardness and microstructure. In that work, the laser power was held constant on each substrate disc while the powder flow rate increased from 10% to 100% of the disc rpm at 10% rpm intervals. These resulted in powder flow rates of 56, 109, 160, 209, 256, 300, 342, 381, 418, and 453 mg/s from the powder hopper. The mass flow rate of the powder from the hopper was directly proportional to the disc rotation. The laser power values were 1000 W, 1200 W, 1400 W, 1600 W, 1800 W and 2000 W, resulting in six substrates with ten clads each for a total of 60 single clads. The scan speed for all experiments was 16.7 mm/s. There was a 120 second dwell time between the deposition of each clad to allow for sufficient cooling.

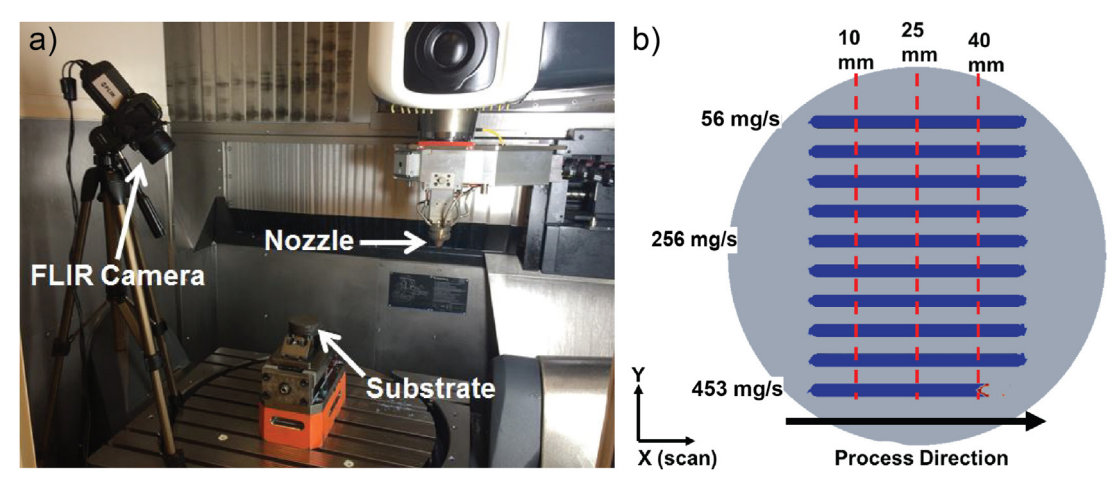


Fig. 2. (a) Experimental setup of the directed energy deposition of the IN718 single clads; (b) the resulting ten clads with increasing powder mass flow on the substrate disc

#### 2.2. Thermal imaging and characterization

During the deposition process, a digital infrared camera calibrated to  $2100\,^{\circ}$ C, the FLIR A655sc, captures thermal images of the melt pool from above at a rate of 24 fps, as seen in Fig. 2. The pixel size of the camera is  $200\,\mu\text{m}$ . In previous work [26], the emissivity of the melt pool was not accurately determined as the material underwent phase transitions, resulting in a temperature reading that was not absolute. Using the thermal images, the trends in cooling rate across the clad and over varying process parameters could be determined at each point. In this work, data points at the 10, 25, and 40 mm cross sections are used for further analysis and comparison. In evaluating the thermal profiles of the single clads, an emissivity value of 0.3 is used to match the parameters in the thermal model as seen in Table 2. Thermal information is extracted from the IR images by thresholding the melt pool pixels and calculating the cooling rate between the liquidus and solidus temperatures [26].

Wire electrical discharge machining separates the substrate discs at the cross sections to view clad dilution into the substrate. After polishing the cross sections, dilution of the solidified melt pool is viewed and measured using optical microscopy. The assumption of measuring the dilution of the resulting clad is that the solidified geometry represents the geometry of the melt pool, or the area within the liquid-solid interface during the process. Vickers microhardness measurements are taken within the clad with a Duramin 5 hardness tester using a press load of 2.94 N for five seconds. At least five points are evaluated for Vickers hardness, ensuring that the gradient, and therefore the heterogeneity of mechanical behavior from the extreme sides of the clad geometry, are captured.

A Kallings etchant [27] is used to etch the clad cross-section to reveal dendrites. Primary (PDAS) and secondary dendrite arm spacing (SDAS) are determined by counting dendrites across ten 100  $\mu m$  lines parallel to primary dendrites. The ten lines parallel to primary dendrites are at different locations within the cross section. The average and standard deviation of PDAS and SDAS are determined for each clad.

#### 3. Computational methods

To consider the complex fluid mechanism of liquid metal and mass addition phenomena, a self-consistent three-dimensional thermo-fluid dynamics model was developed for the DED processing of IN718 clads [13,28]. The non-isothermal Navier–Stokes (N-S) equations, including mass, momentum and enthalpy conservation equations, are solved. A surface profile calculation based on minimizing free surface energy is used to deal with the transient change of top surface due to mass addition. The temperature distribution and liquid metal flow in the melt

pool as well as clad geometry and composition dilution are predicted. The resulting temperature profile provides the solidification parameters, such as the cooling rate between the solidus and liquidus temperatures, that are evaluated to predict the dendrite arm spacing and microhardness distribution of a clad. The model's assumptions follow those in the previous study [29], with the governing equations:

$$\frac{\partial \rho}{\partial t} + \frac{\partial (\rho u_i)}{\partial x_i} = 0 \tag{1}$$

$$\frac{\partial(\rho u_i)}{\partial t} + \frac{\partial(\rho u_i u_j)}{\partial x_j} = \frac{\partial}{\partial x_j} \left( \mu \left( \frac{\partial u_i}{\partial x_j} + \frac{\partial u_j}{\partial x_i} \right) \right) - \frac{\partial \rho}{\partial x_i} - K_0 \frac{(1 - f_l)^2}{f_l^3 + B} u_i + \rho g_i \beta (T - T_{\text{ref}})$$
(2)

$$\frac{\partial(\rho h)}{\partial t} + \frac{\partial(\rho u_i h)}{\partial x_i} = \frac{\partial}{\partial x_i} \left(\frac{k}{c_p} \frac{\partial h}{\partial x_i}\right) - \frac{\partial(\rho L f_l)}{\partial t} - \frac{\partial(\rho u_i L f_l)}{\partial x_i} + S_e$$
(3)

where t is the time,  $u_i$  is the ith component of velocity,  $\mu$  is the viscosity, p is pressure, h is the enthalpy, which is related to the temperature T,  $c_p$  is the specific heat capacity,  $\rho$  is the density, and k is the thermal conductivity.  $K_0$  is the morphology parameter of the porous media, which depends on primary dendrite arm spacing [30].  $K_0$  is 0.24 kg/( $m^3$ · s) in this case. B is a small parameter to avoid dividing by zero, which is  $10^{-3}$  in this study [29]. L is the latent enthalpy of fusion,  $f_l$  is volume fraction of liquid phase, and  $\beta$  is the thermal expansivity. The thermo-physical parameters used in this work are assumed to be constant. The thermal boundary condition at the liquid-gas interface is shown as:

$$q_{\text{ener}} = \frac{2Q(1 - \eta_p)\eta_l}{\pi r_b^2} \exp(\frac{-2((x - Vt)^2 + y^2)}{r_b^2}) - h_c(T - T_{\infty}) - \sigma_c \varepsilon (T^4 - T_{\text{ref}}^4)$$
(4)

where Q is the laser power,  $\eta_p$  and  $\eta_l$  are the absorptivity of powder flow and base metal, respectively. The laser beam radius is  $r_b$ , V is the scanning speed,  $h_c$  is the convective heat transfer coefficient,  $T_\infty$  is the ambient temperature,  $\sigma_s$  is Stefan–Boltzmann constant,  $\varepsilon$  is emissivity [31]. The reference temperature is  $T_{ref}$ . It is noted that the part of energy absorbed by the powder flow returns to the melt pool. Thus, the energy absorbed by the laser-powder interaction is formulated as a source term,  $S_e$ , in the enthalpy equation:

$$S_e = \frac{2Q\eta_p}{\pi r_b^2 d} \exp(\frac{-2((x - Vt)^2 + y^2)}{r_b^2})$$
 (5)

where d is the depth of the melt pool and the source term,  $S_e$ , is determined by iteration with the change of depth.

The metal absorptivity  $\eta_l(T)$  in Eq. (4) is estimated based on the

Hagen-Rubens relationship as follows [32]:

$$\eta_l(T) = (8\varepsilon_0 \omega R_e(T))^{1/2} \tag{6}$$

where  $\omega$  is the angular frequency of the laser and  $\epsilon_0$  is the permittivity of free space. The resistivity  $R_e(T)(\mu\Omega/m)$  for Ni-Fe alloys can be shown as follows [33]:

$$R_e(T) = \begin{cases} -0.96 + 0.005T - 3.919 \times 10^{-6}T^2 + 9.713 \times 10^{-10}T^3, & \text{for solid} \\ 1.251 + 1.364 \times 10^{-4}T, & \text{for liquid} \end{cases}$$
(7)

The absorptivity of in-flight powder flow is difficult to obtain directly from experimental measurement. Hence, in this work, it is used as a calibration parameter, for which the detailed calibration procedure is described in Section 4.2. Boundary condition at the liquid-gas interface for momentum conservation equations are [29]:

$$F_{L/G} = \gamma \mathbf{n} \kappa + \nabla_{S} T \frac{d\gamma}{dT}$$
(8)

where  $\gamma$  is the surface tension of melt pool,  $\boldsymbol{n}$  is the outward normal of the surface, and  $\kappa$  is the curvature of the surface. Previous work [29] detailed the simplified equations to capture the dynamic surface profile of the melt pool. The compositions of IN718 and AISI1045 are listed in Table 1 . The thermal properties of the IN718 powders and the 1045 carbon steel substrate discs are listed in Table 2. Since the medium carbon steel substrate and added Ni-based superalloy powder are mixed in the melt pool during the process, the material properties of melt pool depend on the material properties of the base metal and added powder. Because the composition distribution in the melt pool has been proven to be uniform when the melt pool is fully developed [29], the thermal-physical properties of the thermal-CFD solutions are assumed to follow a simple rule of mixture:

$$A_{\text{solu}} = DA_{\text{sub}} + (1 - D)A_{\text{powd}} \tag{9}$$

where  $A_{solu}$  is the material property used in the solver,  $A_{sub}$  and  $A_{powd}$  are the thermo-physical properties of the substrate and powder, respectively. A can be substituted by the liquid density, liquid thermal conductivity, liquid specific heat capacity, and viscosity. D is the composition dilution representing the weight of the substrate melted divided by the total weight of the melted metal, which is defined in Eq. (15). The dilution value is iterated at each time step.

The Hunt relation is used to evaluate the dendrite arm spacing in the DED process [37]. The primary dendrite arm spacing (PDAS),  $\lambda_p$ , and secondary dendrite arm spacing (SDAS),  $\lambda_s$ , are approximated as follows:

$$\lambda_p = A (k \Gamma \Delta T_0 D_l)^{0.25} G^{-0.5} R^{-0.25}$$
(10)

$$\lambda_s = B(C_R)^{-n} \tag{11}$$

where G, R and  $C_R$  are the thermal gradient, solidification rate and cooling rate at liquid–solid interface of melt pool, respectively. They are calculated from the thermal-fluid simulation. The partition coefficient is k,  $\Gamma$  is the Gibbs Thomson coefficient,  $\Delta T_0$  is the equilibrium freezing range, which is difference between liquidus and solidus temperature, and  $D_l$  is the liquid diffusivity. These physical parameters for Inconel 718 and AISI 1045 can be found in [38–41].The material constants, A, B and n, are 2, 34, 0.25 for Inconel 718 and 0.66, 49, 0.35 for AISI 1045, respectively. Eqs. (10) and (11) can be used to evaluate dendrite arm

**Table 2**Thermo-physical properties of IN718 and AISI 1045 carbon steel [34–36].

Name	Property	IN718 Value	AISI1045 Value
Solid density	$\rho_s (kg \cdot m^{-3})$	7734	7872
Liquid density	$\rho_l  (\text{kg·m}^{-3})$	7578	7700
Solidus temperature	$T_s$ (K)	1533	1713
Liquidus temperature	$T_l$ (K)	1609	1768
Solid specific heat capacity	$c_{ps}$ (J·kg <sup>-1</sup> ·K <sup>-1</sup> )	435	586
Liquid specific heat capacity	$c_{pl}$ (J·kg <sup>-1</sup> ·K <sup>-1</sup> )	755	746
Solid thermal conductivity	$k_s (W \cdot m^{-1} \cdot K^{-1})$	11.4	50.9
Liquid thermal conductivity	$k_l (W \cdot m^{-1} \cdot K^{-1})$	31.3	50.9
Latent heat of fusion	$L (kJ\cdot kg^{-1}\cdot K^{-1})$	290	290
Dynamic viscosity	μ (Pa·s)	$5.30 \times 10^{-3}$	$5.30 \times 10^{-3}$
Thermal expansivity	β (1/K)	$1.3 \times 10^{-5}$	$1.51 \times 10^{-5}$
Surface tension	$\gamma (N \cdot m^{-1})$	1.8	1.8
Marangoni coefficient	$\frac{d\gamma}{dT}$ (N·m <sup>-1</sup> ·K <sup>-1</sup> )	$-3.7 \times 10^{-4}$	$-4.3 \times 10^{-4}$

spacing of Inconel 718 or AISI 1045. However, the Inconel 718 powder mixes with the melted substrate in the melt pool in this case. The dendrite growth is affected by the composition of liquid at the dendrite tip [42]. A plausible assumption is that the parameters in Eqs. (10) and (11) vary with the composition near the mushy zone of melt pool. The computed dilution D reflect the composition in the melt pool due to the assumption of uniform composition profile in the melt pool [13]. As a first order approximation, we assume the actual dendrite arm spacing  $\lambda_{actual}$  of a solidified clad depends linearly on the computed dendrite arm spacing of the substrate  $\lambda_{sub}$  and added powder material  $\lambda_{powd}$  as shown below:

$$\lambda_{\text{actual}} = D\lambda_{\text{sub}} + (1 - D)\lambda_{\text{powd}} \tag{12}$$

The interpolation coefficient is dilution D.  $\lambda$  may represent either PDAS or SDAS. It is noted that Eq. (12) is naturally valid when D is equal to 0 or 1.

The Vickers hardness (HV) can be estimated by the nickel equivalent  $Ni_{EQ}$  for Ni-based superalloys. A form of the  $Ni_{EQ}$  combines with a constrained multivariate linear regression analysis to the elements in IN718 [14]. The expression of  $Ni_{EQ}$  is shown below:

$$Ni_{EQ} = Ni + 0.65Cr + 0.98Mo + 1.05Mn + 0.35Si + 12.6C - 6.36Al + 3.8B + 0.01Co + 0.26Fe + 7.06Hf + 1.2Nb + 4.95Ta + 5.78Ti + 2.88W$$
 (13)

The relation between as-deposited microhardness and  $Ni_{EQ}$  is for Ni-based superalloys based on experimental datasets [14]. The expression is examined to be valid in the maximum concentration of Fe 24.7 wt%. However, the concentration of Fe is much higher than 24.7 wt% for most of cases in this study due to the dilution of the carbon steel substrate. In this study, the relation between microhardness and  $Ni_{EQ}$  is fitted based on three data points: a laser power of 1000 W with a mass flow rate of 56 mg/s, a laser power of 2000 W with a mass flow rate of 56 mg/s, and a laser power of 2000 W with a mass flow rate 453 mg/s. Other datasets are used for validation. The final expression is shown to be.

$$HV = 1.8Ni_{EO} + 112 \tag{14}$$

which can be used in additive manufactured Ni-based superalloy onto carbon steel.

Twenty-five simulation cases of singe track laser deposition are

Table 1
Material composition of IN718 and AISI 1045 by wt%

Material	Fe	Ni	Cr	Nb	Мо	Ti	Al	Co	С	Mn	S
IN718 AISI1045	Bal Bal	50–55 -	17–21 -	4.8–5.5 -	2.8–3.3	0.7–1.2	0.2–0.8	1.0	0.1 0.5	0.4 0.8	0.4 0.04

**Table 3** Process parameters used in CtFD model.

Name	Parameter	Value
Laser power	Q (W)	1000, 1250, 1500, 1750,
		2000
Beam radius	$r_b$ (mm)	1.5
Powder flow radius	$r_p$ (mm)	3
Scan speed	$V \text{ (mm·s}^{-1})$	16.7
Ambient temperature	$T_{\infty}$ (K)	295
Reference temperature	$T_{ref}$ (K)	295
Convection coefficient	$h_c (W \cdot m^{-2} \cdot K^{-1})$	100
Stefan-Boltzmann constant	$\sigma_s(W \cdot mm^{-2}K^{-4})$	$5.67 \times 10^{-14}$
Emissivity	$\varepsilon$	0.3
Permittivity	$\epsilon_0 \ (\text{F} \cdot \text{m}^{-1})$	$8.85 \times 10^{12}$
Angular frequency	$\omega$ (rad·s <sup>-1</sup> )	$1.75 \times 10^{15}$
Mass flow rate	$m_r  (\text{mg·s}^{-1})$	56, 140, 223, 338, 453
Powder catchment efficiency	$\eta_m$	0.9

numerically simulated using an in-house computational thermo-fluid dynamics code called the CtFD model. The laser power values are 1000 W, 1250 W, 1500 W, 1750 W and 2000 W. At each level of a fixed laser power, the powder flow rate increases from 56 mg/s to 453 mg/s at 56 mg/s increments for a total of 25 simulation cases as shown in Table 3. The computational domain is 20 mm  $\times$  10 mm  $\times$  10 mm, with grid discretization of  $210 \times 105 \times 105$  (total 2,315,250 cells). The parameter values in the simulation are listed in Table 3. The simulation time in this study is 1000 ms with a time step of 0.1 ms. The melt pool achieves steady state at 1000 ms based on trial calculation. In each time step, the Navier-Stokes (N-S) and enthalpy conservation equations (Eqs. (1)-(3)) with latent enthalpy of phase change are solved iteratively. Based on the temperature field, a physics-based model provides the melt pool surface profile above the substrate [29]. The surface profile allows the grid to fit the melt pool geometry change, with an additional iteration of the computation of the conservation for the new structure. After the melt pool temperature achieves steady state, dilution, PDAS, SDAS, and microhardness are evaluated based on the thermal profile in the melt pool using Eqs. (10)-(14). The proposed computational methods provide consistent and efficient tools to evaluate the thermal behavior and cooling rate in the melt pool considering

the fluid flow and powder addition. Further, the dendrite arm spacing and microhardness are evaluated based on simplified equations with experimental calibration.

#### 4. Results and discussion

The process–structure–property relationships are discussed in the following subsections. Section 4.1 discusses the influence of processing conditions on temperature and cooling rate. Temperature calculations provide the determination of melt pool geometry and the calibration of laser absorptivity (4.2). Discussion on the comparison of results are provided for clad dilution (4.3), microstructure (4.4), and microhardness (4.4). The experimental results, simulation results, and relationship trends are discussed in each subsection.

#### 4.1. Temperature and cooling rate

The experimental cooling rate between the solidus and liquidus temperatures is determined from IR thermal images at the surface of each clad. Though the IR images do not provide absolute temperature, the cooling rate trends are assumed to reflect the cooling behavior within the melt pool. Currently, experimental determination of cooling rate is restricted to clad surface measurements and at coarse frame rates. To capture the convection forces and melt pool interface within the clad, *in-situ* monitoring techniques that penetrate through the thickness of the material would be required. However, such techniques are time consuming and costly whereas parallelized computational models can provide online monitoring information on thermal histories and predict properties.

By considering the dominant fluid mechanisms of liquid metal in the melt pool, transport phenomena and solidification parameters are obtained and evaluated for the CtFD model. The results of the CtFD model demonstrate the solidification cooling behavior within the melt pool and its liquid-solid front within the substrate. Temperature and velocity evolution within the moving clad processed with different powder mass flow rates with 2000 W laser power are shown in Fig. 3. Temperature and velocity evolution within the moving clad processed with varying laser powers with 56 mg/s powder flow are shown in Fig. 4. As shown in Fig. 3(b) and 4 (b), the flow pattern in the melt pool is outward due

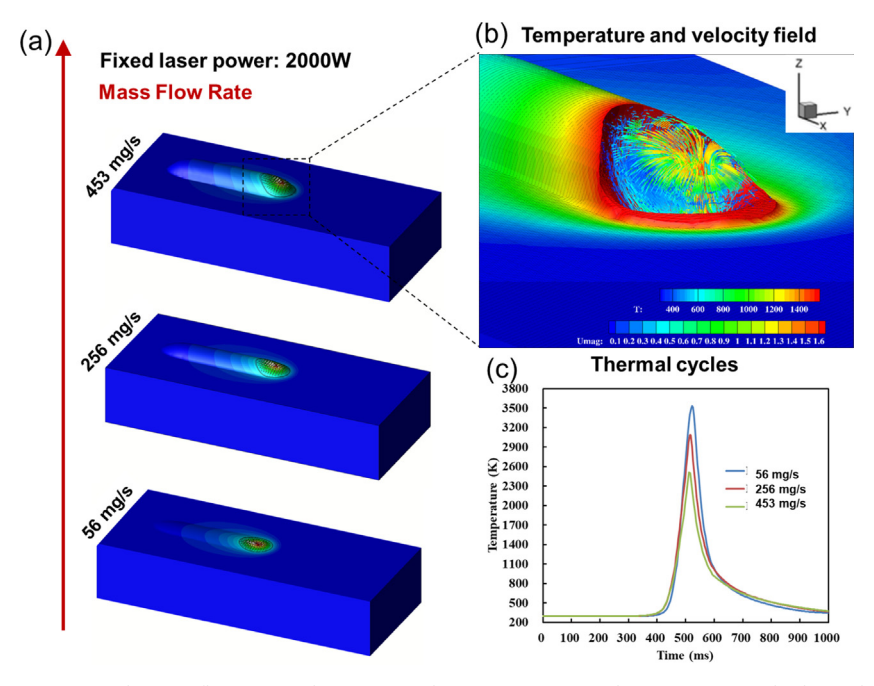


Fig. 3. Simulation cases with increasing powder mass flow rates and 2000 W: (a) deposition geometry; (b) temperature and velocity distributions in the melt pool; (c) thermal cycles at the surface center line.

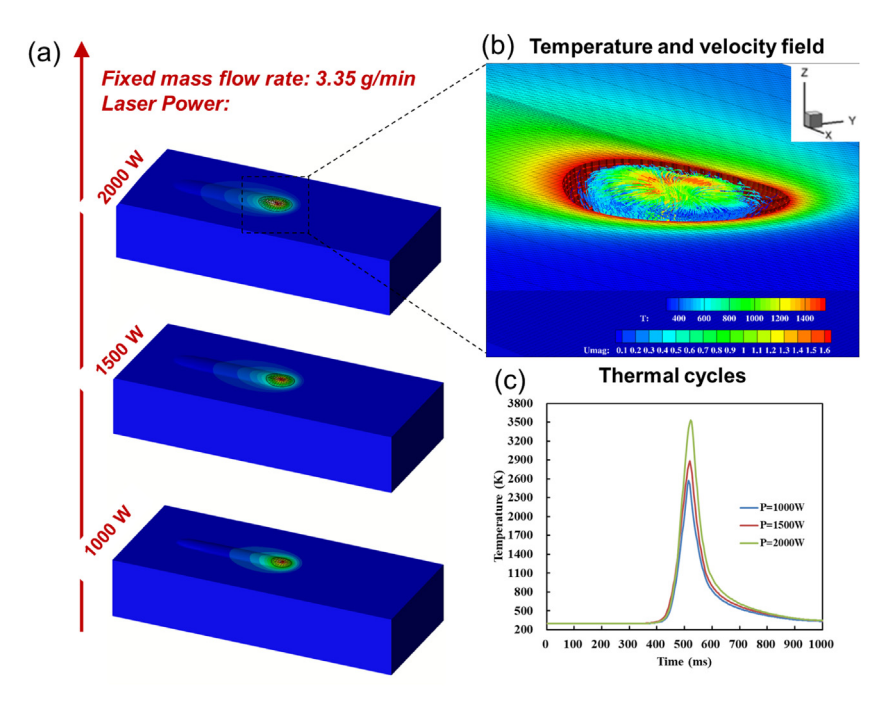


Fig. 4. Simulation cases with increasing laser power with 56 mg/s: (a) deposition geometry; (b) temperature and velocity distributions in the melt pool; (c) thermal cycles at the surface center line.

to a negative surface tension gradient at the surface of melt pool. The color of a streamline represents the magnitude of velocity field. The magnitude of velocity at the top surface is larger than that in other parts of melt pool. The liquid metal flow in the melt pool can significantly affect the thermal distribution in and near the melt pool.

The proposed CtFD determines the temperature gradient (G) and the growth rate (R) at the mushy zone of melt pool, which drive solidification. These thermal parameters influence the microstructure at the liquid-solid interface. As detailed in [29], G is the temperature gradient normal to the liquid-solid front and R is the liquid-solid front velocity. The cooling rate at liquid-solid interface  $(C_R)$ , defined as  $G \times R$ , affects the grain and dendrite size and therefore the properties. For example, lower cooling rates lead to coarser grain sizes.

The comparison of cooling rates determined from surface IR thermography during experiments with simulation-determined cooling rates is shown in Fig. 5. As shown in Fig. 5, increases of both laser power and mass flow rate lead to the decrease of cooling rate. Higher laser power leads to a larger melt pool and lower temperature gradient,

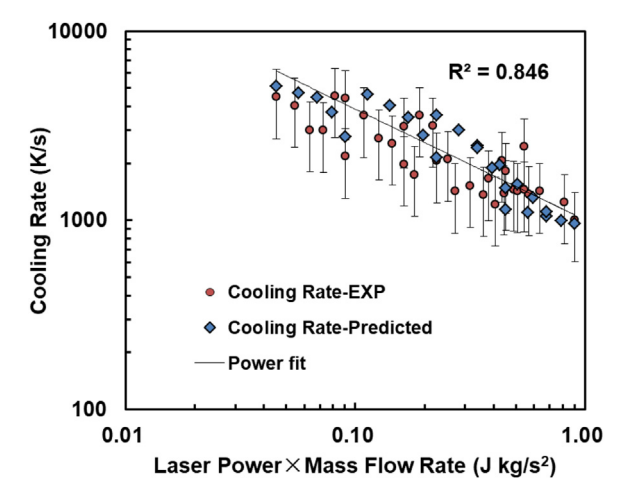


Fig. 5. Comparison of experimentally-determined with simulation-determined cooling rates.

which result in lower cooling rate at the liquid-solid interface of the melt pool. Higher mass flow rate results in more mass per second into the melt pool, which reduce the melt pool peak temperature and cooling rate. As the liquid metal convection is considered in the numerical model, the strong Marangoni convection in the melt pool significantly decreases the cooling rate at the liquid-solid interface.

#### 4.2. Melt pool geometry and absorptivity calibration

The laser absorptivity of in-flight powder and of the underlying substrate are crucial to impact the temperature and velocity distributions in the model-determined melt pool. However, the absorptivity of in-flight powder flow is difficult to obtain from experimental measurements and can be significantly affected by many factors. These factors include shielding gas flow, carrier gas flow, powder flow distribution, laser energy distribution within the beam, and the structure of powder feeding device.

In this work, the absorptivity of in-flight powder is calibrated by fitting the experimental cross section width of the solidified melt pool at four experimental conditions: 1000 W, 56 mg/s; 1000 W, 453 mg/s; 2000 W, 56 mg/s and 2000 W, 453 mg/s. During the calibration procedure, a series of cases is run with interval absorptivity of in-flight powder for each condition. Then, the calculated melt pool width for each case is compared with the experimental clad width. The closest predicted melt pool width to the experimental clad width is the calibrated absorptivity value of in-flight powder. This procedure is repeated for the four process conditions. The values at other process parameters are interpolated from these four points. The results of the calibration with changing laser power and powder mass flow rates are shown in Fig. 6(a). The absorptivity of in-flight powder substantially increases with the increase in powder mass flow rate within the processing conditions used for calibration. This implies that a greater amount of laser energy is absorbed by the in-flight powder when the powder mass flow increases due to the block of powder flow above the melt pool. The increase of laser power also causes a slight increase in the absorptivity of the in-flight powder. The range of absorptivity values of in-flight powder is from 0.11 to 0.39 when using industrialgrade processing conditions. This is comparable to the absorptivity of

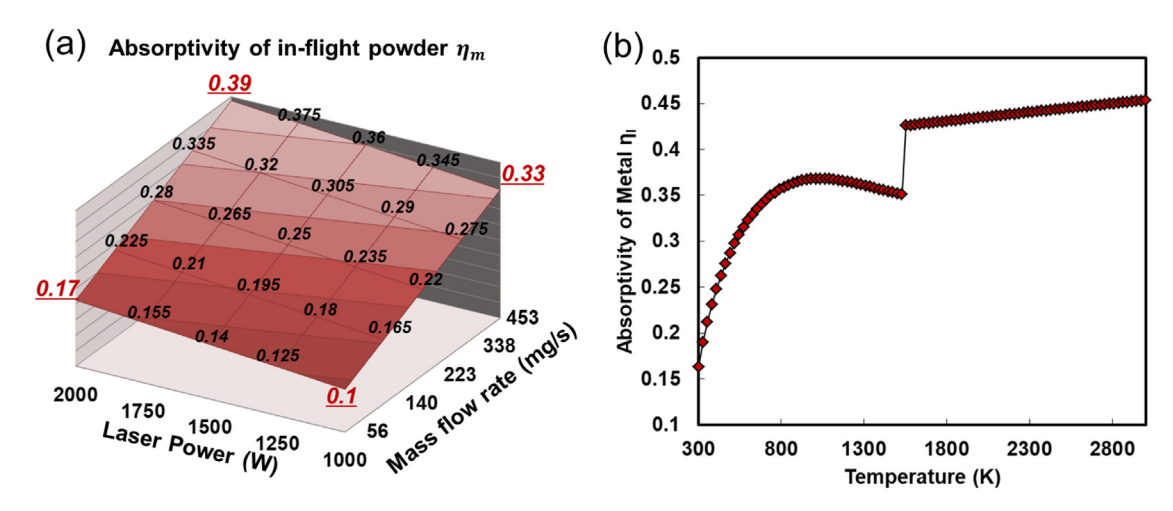


Fig. 6. Absorptivity used in the CtFD model: (a) of in-flight powder; (b) of base material for Ni-Fe alloys.

Ni-Fe base material of the powders calculated by Eq. (6) using the constants given in [33], as shown in as shown in Fig. 6(b). At the melting point of the Ni-Fe base material, the absorptivity of the material increases linearly.

The comparisons of cross section geometries, including width, depth and shape, between simulation and experimental results with calibrated absorptivity parameters are shown in Fig. 7. The calculated melt pool geometries with the temperature-dependent absorptivity at both laser powers of 1000 W and 2000 W agree well with the experimental cross section results. The quantitative comparison will be reported later in Section 4.3. The good agreement implies that the proposed numerical model can be beneficial in capturing the overall interaction between the laser and the in-flight powder. This aids in the understanding and designing of multi-physics processes that occur in DED. The deviation between numerical and experimental results can possibly be ascribed to the assumptions of the temperature-independent thermal properties and Gaussian laser flux distribution.

#### 4.3. Clad dilution

Varying process parameters such as the powder mass flow rate at constant laser power and scanning speed results in a change in the cross sectional shape of the solidified clad [43,44]. This area can be

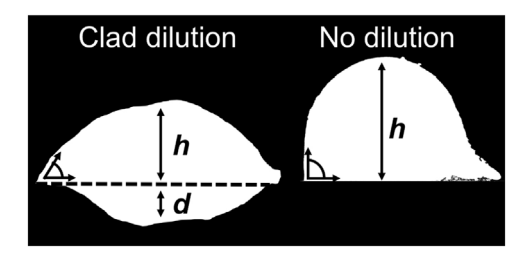


Fig. 8. Schematic of clad dilution.

characterized by the dilution of the melt pool into the substrate or the previously built layer as seen in Fig. 8. Dilution, *D*, is defined by [45]:

$$D = \frac{d}{h+d} \tag{15}$$

where h is the clad height above the substrate and d is the depth below the substrate.

Dilution can be used to quantify the bond between the melted, deposited material and the substrate [45]. Dilution also elucidates the amount of laser attenuation by powder flow during the process. Substantial dilution ratios vary with deposited and substrate material. Dilution of Inconel clads onto steel substrates that are greater than about

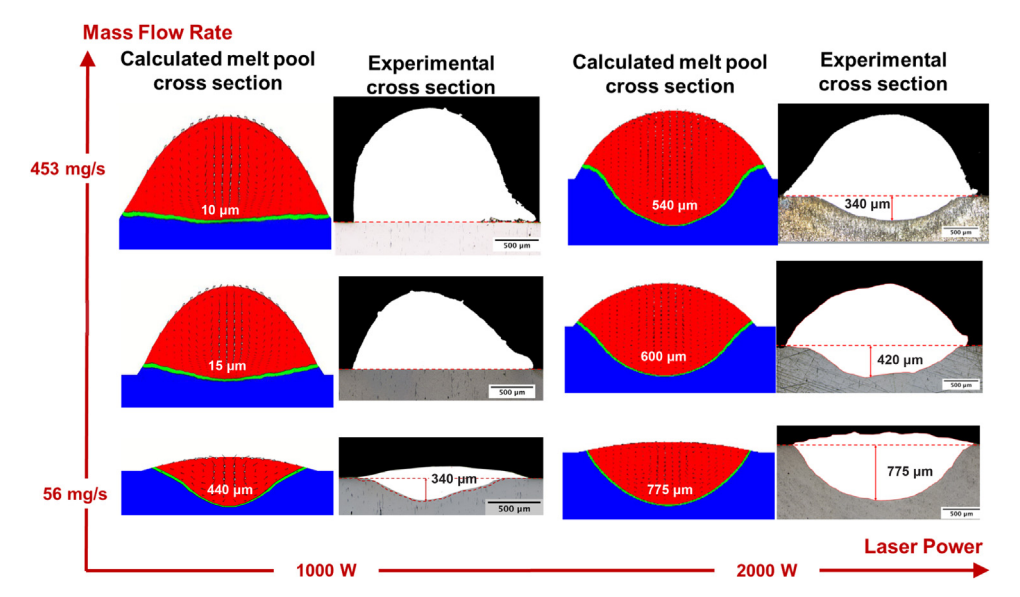


Fig. 7. Comparisons of cross section geometry between simulation and experimental results at various laser power and powder mass flow rates.

0.6 indicates excessive melting of the substrate material that cannot pass qualification standards [46]. During cladding of powder onto a substrate of a dissimilar material, minimal dilution is preferred to stabilize gradients in chemical composition [47]. In a study on the dilution of laser-cladded γ-TiAl intermetallic powders onto a titanium alloy substrate [48], low dilution values of 0.06 were optimal for high microhardness properties. In multi-layer builds, low dilution between layers contribute to lack of fusion, with a dilution ratio of at least 0.15 required for substantial bonding in a study of laser deposited Ti-6Al-4V powders onto a Ti-6Al-4V substrate [49]. However, these threshold values are flexible and can be compensated for by adjusting the layer thickness when building multi-layer structures. The dilution ratio of a melt pool depends on the material's thermal properties like conductivity, expansion, absorption, surface tension and chemical composition, etc., relative to the properties of the underlying layer or substrate.

For powder-blown additive manufacturing, powder mass flow rates influence the geometry and dilution of a clad. Several studies have found that the thermal history and the cooling rate of the melt pool have a direct influence on the amount of dilution in additive processing [44,26]. Melt pool depth and dilution have a nonlinear relationship with process parameters [50]. In this work, the clads have relatively high dilution ratio values of greater than 0.5. These dilution ratios correspond with IR thermography-determined cooling rates at the clad surface of greater than 4000 K/s. This relationship suggests that the majority of the relatively low mass powder flow enters the melt pool and mixes with the substrate at a high amount of energy density at the solidification front, or liquid–solid interface, at any given time.

The experimentally-determined geometrical dilution of the clad cross-sections increases with increasing cooling rates determined from IR images when they are processed with the same laser power. Experimentally-determined cooling rates between solidus and liquidus temperatures,  $\hat{T}$  (K/s) are normalized to the process parameters of laser power per unit of mass powder flow per second, as seen in the equation:

$$\hat{T} = \dot{T}/(Q/m_r) \tag{16}$$

where  $\hat{T}$  is the normalized cooling rate between solidus and liquidus temperatures, Q is the laser power, and  $m_r$  is the powder flow rate. With increasing normalized cooling rate,  $\hat{T}$ , clad dilution decreases and reaches zero after a threshold of about 0.4 K·g·J<sup>-1</sup>·s<sup>-1</sup>, as seen in Fig. 9. The clads with zero dilution occur when the powder flow rate is above the threshold relative to the laser's input energy. For example, at 1200 W processing power, dilution occurs in the experimental clads only when the powder flow rate is less than 209 mg/s, or 40% disc rpm, whereas there is dilution for every powder flow rate at 2000 W processing power. Fig. 9 also shows that at relatively high cooling rates and high powder flow, there is less mixing of liquid IN718 into the substrate

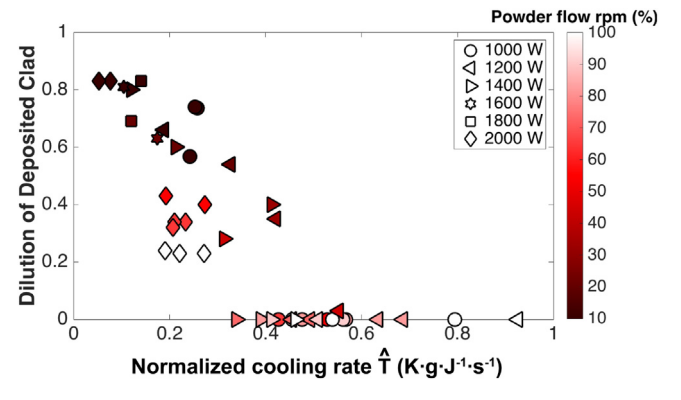


**Fig. 9.** Experimentally determined dilution values of single line clads and their corresponding cooling rates determined by surface IR thermography normalized by laser power divided by mass powder flow rate, or  $\hat{T}$  as denoted in Eq. (16).

depth. In these conditions, most of the powder solidifies above the substrate surface and exhibits shrinkage at the liquid-solid interface. Both the Marangoni convection within the melt pool and increased laser attenuation due to high powder flow lead to decreased cooling rates at the surface of the melt pool.

Another metric to capture the laser-matter interaction in the process is the energy density per unit of mass. Because the laser scan speed of each clad is kept constant at 16.7 mm/s, this metric compares the influence of the laser power and powder flow, similarly to the powder density used in previous dilution studies [48]. The energy density metric also compares the dilution results from both experimental and the CtFD model. Energy density is used to scale the relation between dilution and process parameters, with the definition of energy density as follows:

$$E_D = \frac{Q}{m_r} \tag{17}$$

Fig. 7 shows no dilution of clads when the mass powder flow is 256 mg/s or greater with 1000 W laser power, amounting to energy densities of less than  $4.5 \times 10^6$  J/kg. An increased powder flow attenuates the laser, leading to in-flight particles absorbing the laser energy. Reducing the blocking powder flow or increasing laser power can increase dilution. With a high powder flow of 453 mg/s and low laser power of 1000 W, there is only partial adhesion of the clad onto the substrate and a potential crack forming at the clad-substrate interface. With an increase in energy density at the melt pool, dilution into the substrate increases and with greater efficiency of powder melting as seen in Fig. 10. Fig. 10 plots both the experimental and CtFD-determined dilution ratios, with both sets of results matching well. When the energy density input is less than the critical energy density,  $4.5 \times 10^6$  J/kg, there is no dilution. When the energy density is greater than the critical value, dilution increases logarithmically.

#### 4.4. Microstructure and microhardness

Thermal properties such as cooling rate dictate the geometry of the melt pool and the solidified clad. The trends in cooling behavior dictate the trends in changing microstructure, and therefore the mechanical behavior within the clad. Localized primary (PDAS) and secondary dendrite spacing (SDAS) throughout the clad are determined to compare the experimentally-determined microstructure to the cooling rates between solidus and liquidus temperatures calculated from IR thermography. The dendrite spacing varies with depth in the clad and proximity to the clad surface, with an example of the dendritic structure in Fig. 11.

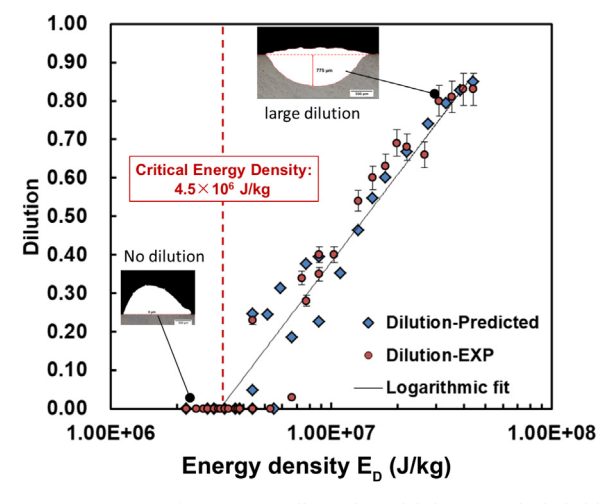


Fig. 10. Comparison of experimentally and model-determined clad dilution values with energy density,  $E_D$ , as denoted in Eq. (17).

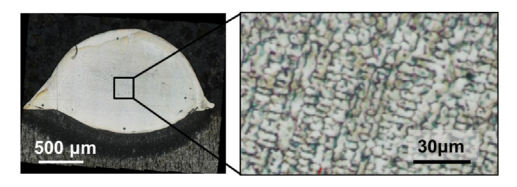


Fig. 11. Example of secondary dendrite spacing within the clad cross section.

Spacing values at the center of the clad are evaluated for trends and model prediction. Overall trends indicate that dendrite arm spacing decreases with decreasing powder mass flow rates. This corresponds with the increasing cooling rates observed in IR camera monitoring of clads with decreasing powder mass flow rate in a previous study [26]. As seen in Fig. 12, PDAS and SDAS from experiments and the CtFD model decrease as functions of power with the increase of the energy density,  $E_D$ . The dendrite arm spacing from experimentally determined microstructures correspond to the numerically simulated conditions with the same laser power, scan speed, and powder flow rate. Therefore, three experimental settings with a total of thirty dendrite arm spacing measurements experiments are considered to be representative. It is well known that increasing cooling rate corresponds to refined dendrite arm spacing. Because there is substantial correlation between the experimentally-determined cooling rates from IR thermography and the models cooling rate calculations as seen in Fig. 5, the resulting experimentally-determined dendrite spacing also match the models dendrite spacing as the dendritic spacing are related to the cooling rate. The goodness of fit values for the statistical model as shown in Fig. 12 are 0.7887 for primary dendrite arm spacing in Fig. 12(a) and 0.8444 for secondary dendrite arm spacing in Fig. 12(b).

It has been reported that microhardness of the laser-deposited clad depends on its morphology and size of dendrite arm [17], precipitation strengthening of  $\gamma$ ' [51], and alloy composition [52]. The high temperature toughness and ductility of IN718 are provided by the face-centered cubic (FCC) nickel crystal structure ( $\gamma$ -phase) matrix [53]. The precipitation strengthening of,  $\gamma$ " to the  $\gamma$  matrix and the intercrystal-line strengthening of platelet-like  $\delta$  phase to the grain boundaries contribute to increased microhardness [51]. Other possible precipitates during phase transformations of IN718 include carbides and the eutectic Laves phase, which is known to be detrimental to the mechanical properties of IN718 [53].

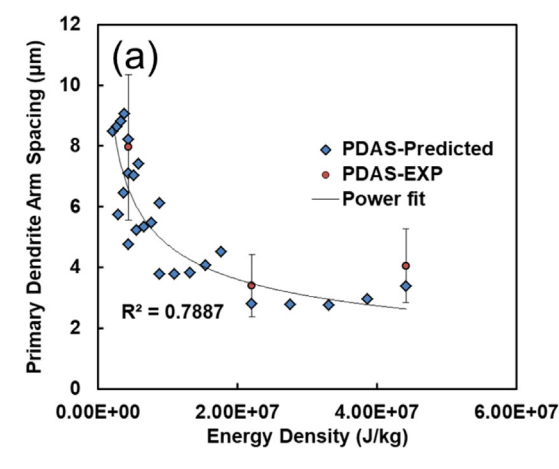
In this work, we examined the roles of cooling rate, i.e. the product of G and R, and alloy composition on the microhardness in laser deposited IN718 on 1045 carbon steel. Cooling rates calculated from IR thermography vary dramatically from the solidification region and at lower cooling temperatures where  $\gamma'$  and  $\gamma''$  precipitation strengthening

may occur [54]. Because of varying microhardness values within the clad cross-section and the sensitivity of the IR thermography-determined cooling rates, the microhardness values along the top of the clad are used. The microhardness measurements at the clad surface are more indicative of the surface IR temperature readings. The results in Fig. 13 are averages of multiple microhardness measurements along the top of the clad, or close to the surface.

Variation of microhardness as a function of cooling rate and alloy composition represented by Ni equivalent is shown in Fig. 13(a) and (b), respectively. Although several reports have shown that an increase in cooling rate leads to grain/dendrite arm refinement and suppresses the Laves phase and Nb microsegregation [55,51], resulting in greater microhardness, in this work we find that alloy composition, rather than cooling rate, dominates the variation of microhardness in laser deposited IN718 on 1045 carbon steel. As shown in Fig. 13(a), there is no considerable relation between cooling rate and microhardness. Although a higher cooling rate leads to finer dendrite arm spacing, some data points with high cooling rates but low microhardness can be found in Fig. 13(a). A low  $R^2$  (0.1887) also indicates a weak correlation between cooling rate and microhardness. Ni equivalent values for three points with the same level of cooling rate (around 3100 K/s) are also marked in Fig. 13(a). The Ni equivalent is calculated based on the alloy composition of the mixed powder and substrate, as well as the dilution during the process using Eq. (13).

At the same level of cooling rate, a large fluctuation of microhardness is shown due to the influence of alloy composition. A noticeable linear correlation between Ni equivalent composition and microhardness is shown in Fig. 13(b), where the microhardness increases with the increase of Ni equivalent. At the maximum Ni equivalent values that correspond to clads with zero dilution, clads exhibit the highest microhardness. A higher  $R^2$  (0.8306) indicates a good linear correlation. Because the powder and substrate are different materials with different compositions (Ni-based and iron-based alloys) and average hardness (IN718-300 HV and carbon steel-150 HV), mass transfer and composition mixture of two materials in the melt pool play a vital role on microhardness. This implies that a good prediction of microhardness relies on an accurate dilution prediction. From the results, we state that the variation of microhardness is dominated by the alloy composition mixture, rather than cooling rate, in single track laser-deposited IN718 on 1045 carbon steel with the cooling rate range (1000-4000 K/s) and the dilution range (0-0.9).

Fig. 14 shows the calculated microhardness with the experimentally-determined microhardness values. The predicted microhardness is calculated using Eqs. (13) and (14). With the exception of an outlying clad measurement of about 300 Hv, all the measured hardness values are considerably below the hardness value of conventionally processed



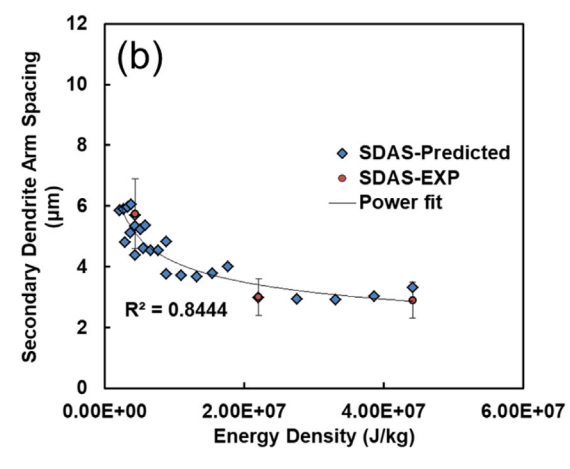
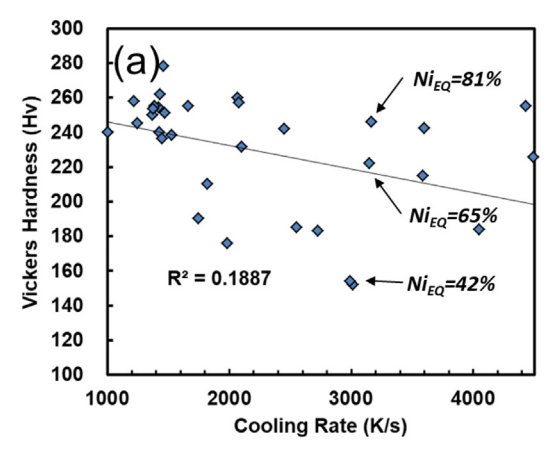


Fig. 12. Relationships of experimentally and model-determined average dendrite arm spacing with energy density,  $E_D$ : (a) Primary dendrite arm spacing, (b) Secondary dendrite arm spacing.



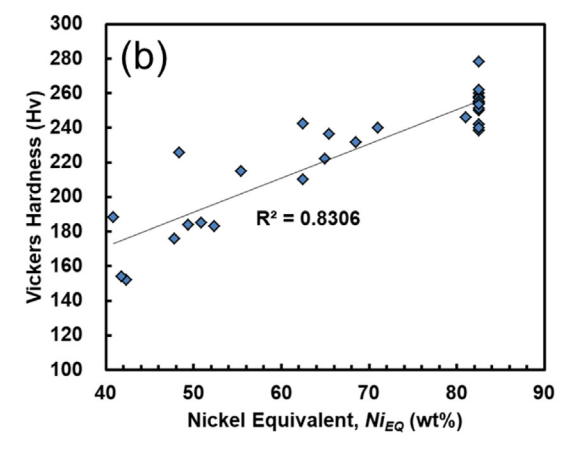


Fig. 13. (a) Relationship between microhardness and cooling rate, (b) Relationship between microhardness and nickel equivalent composition.

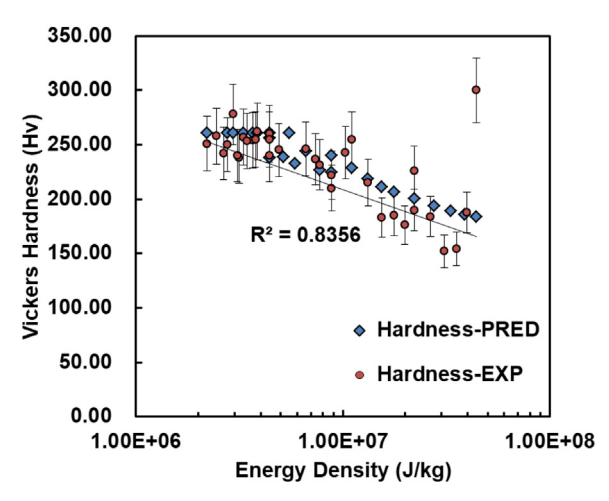


Fig. 14. Comparison of experimentally and model-determined microhardness with energy density,  $E_D$ .

and heat treated IN718 hardness value which is 383 Hv [51]. The outlying hardness value of 300 Hv from the clad is comparable to the conventionally processed IN718 value. In multi-layer builds, this low hardness was observed at the top layer because it only underwent one thermal cycle [56]. It is noted that although the effects of cooling rate and SDAS on hardness are neglected in the microhardness prediction model, an approximate relation between composition (equivalent nickel) and microhardness can be used with reasonable accuracy. That is because rather than variation in SDAS, the composition changes due to composition mixture (dilution effect) dominates the variation in microhardness. The deviation between numerical and experimental results is possibly a result of the non-linear solidification mechanisms such as rapidly quenched segregates, which are not considered in the microhardness analysis module.

A comparison of cooling rates, depths of the clad into the substrate, dilution ratios and microhardness values are summarized in Table 4. The proposed computational thermo-fluid model, the CtFD model, considers physics such as powder mass flow and fluid dynamics of the

**Table 4**Comparison of results from experiments and the thermo-fluidic model.

Property	Experiments	CtFD model
Cooling rate between solidus and liquidus temperature (K/s)	800-6000	800-6000
Clad depth into the substrate (µm)	0-800	0-1000
Clad dilution ratios at 56 mg/s; 1000, 2000 W	0.69, 0.86	0.75, 0.90
Microhardness (Hv)	190-300	180-260

melt pool that capture the cooling rate at the solid-liquid interface of the melt pool with high accuracy. The model also predicts for dendrite arm spacing and microhardness at localized points within a build. The CtFD model is calibrated by using the temperature profiles that determine the dilution and geometries values of the deposited clads. The calibration of experimental results lead to the prediction of microhardness with cooling rate and the dilution ratio of the resulting IN718 clad into the steel substrate. Future work includes incorporating a more detailed dendritic microstructure model to accurately predict other material properties of the resulting material, such as strength and ductility. The future experimental work of determining phase compositions and macro and micro segregation will also further improve the microhardness prediction module.

#### 5. Conclusions and future work

An experimental study of single clads processed with the DED additive manufacturing process with various powder mass flow rates and laser power inputs demonstrates how the laser-material interaction can lead to discrepancies in dilution into the substrate and a change in mechanical properties. Process parameters influence the cooling rate, which ultimately influences the structure and properties. Because process parameters vary with system or machine, normalization was used to determine relationships. Based on IR thermography measurements at the surface of the IN718 clads, an increase of cooling rates normalized to laser power and mass powder flow leads to decreased dilution into the substrate as more conduction into the substrate material and laser scattering with the deposited material occurs. Energy density significantly affects the dilution of a clad. A critical energy density, 4.5 ×10<sup>6</sup> J/kg, is found in this case. Both PDAS and SDAS decrease with energy density based on the power law. Microhardness values initially increase with cooling rates normalized to the amount of laser power for each unit of mass powder flow, then level off at a value of about 250 Hv. The variation of microhardness dominates by the alloy composition mixture, rather than cooling rate, in single track laser-deposited IN718 on 1045 carbon steel with the cooling rate range (1000-4000 K/s) and the dilution range (0-0.9).

The proposed inexpensive and well-tested computational framework can generate a large amount of high-quality prediction data, including temperature field, velocity field, melt pool dimensions, dilution, heating and cooling rates, solidification parameters, and microhardness. To provide a better prediction for AM processing of a miscible dissimilar alloys system, the developed model considers the thermophysical properties changes due to composition dilution. The results show good agreement between model predictions and experimental data.

Future experimental studies will investigate the cooling rates that lead to complex phase transformations and segregation that occur in IN718 that can lead to significant changes in mechanical behavior. To improve the computational models, future work also includes temperature dependent thermal properties from CALPHAD-based methods for more accurate and robust simulations. From the results in this work, a CFD model with a constant powder catchment efficiency can provide good predictions as compared with experimental data for the conditions studied here. However, the powder catchment efficiency can change with varying laser energy input, depending on the temperature dependent thermo-physical properties of the material as it transitions between its liquid and solid phases. Changes in the powder catchment efficiency will introduce discrepancies in melt pool geometry, dilution and cooling rate. More accurate temperature dependent thermo-physical properties could result in greater powder catchment efficiency. possibly also resulting in less dilution and lower cooling rates of the melt pool. Future experiments to validate temperature dependent thermo-physical properties of the IN718 and AISI1045 mixture include using a high-speed infrared camera during the melting and solidification of the combined material. Future work will consider varying powder catchment efficiency based on both in-situ and ex-situ experimental studies. Using in-situ high-speed imaging and acoustic emission techniques, the amount of powder entering the melt pool can be captured by tracking the movement of particles and whether they melt, scatter, or flow outside of the spatial range of the melt pool. Further analysis of clad and dilution geometries with ex-situ characterization can also provide information on powder catchment efficiency with varying processing conditions by comparing the powder material mass in the resulting build versus the mass flow rate of the powder material during deposition.

In addition, the data presented in this work can train a reducedorder model (ROM) to obtain the linkages between processing parameters of the DED-processed build and the resulting mechanical properties. A data-based online monitoring and feedback control modeling approach will be applied to the localized DED process and other relevant multi-scale and multi-physics processes. Data-driven relationships between process and properties can provide online monitoring and process control for desirable cooling rates at localized points to drive ideal phase transformations.

#### Acknowledgements

J. Cao, G. J. Wagner and W. K. Liu acknowledge the support by the National Science Foundation (NSF) Cyber-Physical Systems (CPS) under grant No. CPS/CMMI-1646592. J. Cao, G. J. Wagner, W. K. Liu, J.L. Bennett and S.J. Wolff acknowledge the support by the Digital Manufacturing and Design Innovation Institute (DMDII) through award number 15-07. J.Cao, W. K. Liu, Z. Gan, J.L. Bennett and W. Yan acknowledge the support by Center for Hierarchical Materials Design (CHiMaD) under grant No. 70NANB14H012. S. Lin acknowledges the support by the NSF Graduate Research Fellowship under Grant No. DGE-1324585. This work made use of facilities at DMG MORI and Northwestern University. This work made use of the MatCI Facility which receives support from the MRSEC Program (NSF DMR-1720139) of the Materials Research Center at Northwestern University.

#### References

- [1] S. Wen, Y.C. Shin, Modeling of transport phenomena during the coaxial laser direct deposition process, J. Appl. Phys. 108 (2010) 044908.
- [2] S.J. Wolff, S. Lin, E.J. Faierson, W.K. Liu, G.J. Wagner, J. Cao, A framework to link localized cooling and properties of directed energy deposition (ded)-processed Ti-6Al-4V, Acta Mater. 132 (2017) 106–117.
- [3] S. David, T. DebRoy, Current issues and problems in welding science, Science 257 (1992) 497–502.
- [4] Y. Huang, X. Zeng, Investigation on cracking behavior of Ni-based coating by laser-induction hybrid cladding, Appl. Surf. Sci. 256 (2010) 5985–5992.
- [5] V. Ocelík, U. De Oliveira, M. De Boer, J.T.M. De Hosson, Thick co-based coating on cast iron by side laser cladding: Analysis of processing conditions and coating properties, Surf. Coat. Technol. 201 (2007) 5875–5883.

- [6] S. Zhou, X. Dai, X. Zeng, Effects of processing parameters on structure of ni-based wc composite coatings during laser induction hybrid rapid cladding, Appl. Surf. Sci. 255 (2009) 8494–8500.
- [7] W. Gao, S. Zhao, Y. Wang, Z. Zhang, F. Liu, X. Lin, Numerical simulation of thermal field and fe-based coating doped ti, Int. J. Heat Mass Transfer 92 (2016) 83–90.
- [8] A. Emamian, M. Alimardani, A. Khajepour, Correlation between temperature distribution and in situ formed microstructure of fe-tic deposited on carbon steel using laser cladding, Appl. Surf. Sci. 258 (2012) 9025–9031.
- [9] H. Qi, J. Mazumder, H. Ki, Numerical simulation of heat transfer and fluid flow in coaxial laser cladding process for direct metal deposition, J. Appl. Phys. 100 (2006) 024903
- [10] X. He, J. Mazumder, Transport phenomena during direct metal deposition, J. Appl. Phys. 101 (2007) 053113.
- [11] A. Kumar, S. Roy, Effect of three-dimensional melt pool convection on process characteristics during laser cladding, Comput. Mater. Sci. 46 (2009) 495–506.
- [12] S. Wen, Y.C. Shin, Modeling of the off-axis high power diode laser cladding process, J. Heat Transfer 133 (2011) 031007.
- [13] Z. Gan, G. Yu, X. He, S. Li, Numerical simulation of thermal behavior and multicomponent mass transfer in direct laser deposition of co-base alloy on steel, Int. J. Heat Mass Transfer 104 (2017) 28–38.
- [14] T. DebRoy, H.L. Wei, J.S. Zuback, T. Mukherjee, J. W. Elmer, W. Milewski, J.O. Zhang, Additive manufacturing of metallic componentsprocess, structure and properties, Progr. Mater. Sci. (2018).
- [15] M. Tang, P.C. Pistorius, S. Narra, J.L. Beuth, Rapid solidification: selective laser melting of alsi10mg, JOM 68 (2016) 960–966.
- [16] Y. Liu, Z. Liu, Y. Jiang, G. Wang, Y. Yang, L. Zhang, Gradient in microstructure and mechanical property of selective laser melted alsi10mg, J. Alloys Compd. 735 (2018) 1414–1421.
- [17] R. Acharya, R. Bansal, J.J. Gambone, S. Das, A coupled thermal, fluid flow, and solidification model for the processing of single-crystal alloy cmsx-4 through scanning laser epitaxy for turbine engine hot-section component repair (part i), Metallurgical and Materials Transactions B 45 (2014) 2247–2261.
- [18] R. Acharya, R. Bansal, J.J. Gambone, S. Das, A microstructure evolution model for the processing of single-crystal alloy cmsx-4 through scanning laser epitaxy for turbine engine hot-section component repair (part ii), Metall. Mater. Trans. B 45 (2014) 2279–2290.
- [19] W. Wang, P.D. Lee, M. Mclean, A model of solidification microstructures in nickel-based superalloys: predicting primary dendrite spacing selection, Acta materialia 51 (2003) 2971–2987.
- [20] P. Nie, O. Ojo, Z. Li, Numerical modeling of microstructure evolution during laser additive manufacturing of a nickel-based superalloy, Acta Mater. 77 (2014) 85–95.
- [21] T. Keller, G. Lindwall, S. Ghosh, L. Ma, B.M. Lane, F. Zhang, U.R. Kattner, E.A. Lass, J.C. Heigel, Y. Idell, et al., Application of finite element, phase-field, and calphadbased methods to additive manufacturing of ni-based superalloys, Acta Mater. 139 (2017) 244–253.
- [22] G. Knapp, T. Mukherjee, J. Zuback, H. Wei, T. Palmer, A. De, T. DebRoy, Building blocks for a digital twin of additive manufacturing, Acta Mater. 135 (2017) 390–399
- [23] T. Mukherjee, H. Wei, A. De, T. DebRoy, Heat and fluid flow in additive manufacturingpart ii: Powder bed fusion of stainless steel, and titanium, nickel and aluminum base alloys, Comput. Mater. Sci. 150 (2018) 369–380.
- [24] P. Muller, P. Mognol, J.-Y. Hascoet, Modeling and control of a direct laser powder deposition process for functionally graded materials (fgm) parts manufacturing, J. Mater. Process. Technol. 213 (2013) 685–692.
- [25] M. Vaezi, S. Chianrabutra, B. Mellor, S. Yang, Multiple material additive manufacturing-part 1: a review: this review paper covers a decade of research on multiple material additive manufacturing technologies which can produce complex geometry parts with different materials, Virtual Phys. Prototyping 8 (2013) 19–50.
- [26] J.L. Bennett, S.J. Wolff, G. Hyatt, K. Ehmann, J. Cao, Thermal effect on clad dimension for laser deposited inconel 718, J. Manuf. Process. 28 (2017) 550–557.
- [27] X. Zhao, J. Chen, X. Lin, W. Huang, Study on microstructure and mechanical properties of laser rapid forming inconel 718, Mater. Sci. Eng. A 478 (2008) 119–124.
- [28] Z. Gan, G. Yu, X. He, S. Li, Surface-active element transport and its effect on liquid metal flow in laser-assisted additive manufacturing, Int. Commun. Heat Mass Transfer 86 (2017) 206–214.
- [29] Z. Gan, H. Liu, S. Li, X. He, G. Yu, Modeling of thermal behavior and mass transport in multi-layer laser additive manufacturing of ni-based alloy on cast iron, Int. J. Heat Mass Transfer 111 (2017) 709–722.
- [30] T. Mukherjee, H. Wei, A. De, T. DebRoy, Heat and fluid flow in additive manufacturingpart i: Modeling of powder bed fusion, Comput. Mater. Sci. 150 (2018) 304–313
- [31] Z. Gan, G. Yu, S. Li, X. He, R. Chen, C. Zheng, W. Ning, A novel intelligent adaptive control of laser-based ground thermal test, Chinese Journal of Aeronautics 29 (2016) 1018–1026.
- [32] Y. Lee, et al., Influence of fluid convection on weld pool formation in laser cladding, Weld. J. 93 (2014) 292S–300S.
- [33] G. Pottlacher, et al., Thermophysical properties of solid and liquid inconel 718, Thermochim. Acta 382 (2002) 255–267.
- [34] Anon, http://www.espimetals.com/index.php/technical-data/91-inconel-718 (2019).
- [35] H. Hosaeus, A. Seifter, E. Kaschnitz, et al., Thermophysical properties of solid and liquid inconel 718 alloy, High Temper. High Press. 33 (2001) 405–410.
- [36] J. Elmer, T. Palmer, S. Babu, W. Zhang, T. DebRoy, Direct observations of austenite, bainite and martensite formation during arc welding of 1045 steel using time resolved x-ray diffraction, The Welding Journal 83 (2004) UCRL-JRNL-202445.

- [37] J. Hunt, The metal society, London 3 (1979).
- [38] M.J. Cieslak, et al. The solidification metallurgy of alloy 718 and other nb-containing superalloys, Superalloy (1989) 59-68.
- [39] T.P. Battle, R.D. Pehlke, Equilibrium partition coefficients in iron-based alloys, Metall. Mater. Trans. B 20 (1989) 149–160.
- [40] C. Guminski, Diffusion coefficients in liquid metals at high dilution, In Liquid Metal Systems (1995) 345-356.
- [41] S. Ghosh, L. Ma, N. Ofori-Opoku, J.E. Guyer, On the primary spacing and microsegregation of cellular dendrites in laser deposited ninb alloys, Model. Simul. Mater. Sci. Eng. 25 (2017) 065002.
- [42] J.A. Dantzig, M. Rappaz, Solidification, EPFL press, 2009.
- [43] J. Liu, L. Li, Effects of process variables on laser direct formation of thin wall, Opt. Laser Technol. 39 (2007) 231–236.
- [44] M.H. Farshidianfar, A. Khajepour, A.P. Gerlich, Effect of real-time cooling rate on microstructure in laser additive manufacturing, J. Mater. Process. Technol. 231 (2016) 468-478
- [45] E. Toyserkani, S. Corbin, A. Khajepour, Laser cladding. Crc Press, Boca Raton, Florida (2005).
- [46] C.-M. Lin, Relationships between microstructures and properties of buffer layer with inconel 52m clad on aisi 316l stainless steel by gtaw processing, Surf. Coat. Technol. 228 (2013) 234–241.
- [47] N. Shamsaei, A. Yadollahi, L. Bian, S.M. Thompson, An overview of direct laser deposition for additive manufacturing; part ii: Mechanical behavior, process

- parameter optimization and control, Addit. Manuf. 8 (2015) 12-35.
- [48] I.N. Maliutina, H. Si-Mohand, R. Piolet, F. Missemer, A.I. Popelyukh, N.S. Belousova, P. Bertrand, Laser cladding of γ-tial intermetallic alloy on titanium alloy substrates, Metall. Mater. Trans. A 47 (2016) 378–387.
- [49] T. Mukherjee, J. Zuback, A. De, T. DebRoy, Printability of alloys for additive manufacturing, Sci. Rep. 6 (2016) 19717.
- [50] A. Fathi, E. Toyserkani, A. Khajepour, M. Durali, Prediction of melt pool depth and dilution in laser powder deposition, J. Phys. D: Appl. Phys. 39 (2006) 2613.
- [51] Z. Wang, K. Guan, M. Gao, X. Li, X. Chen, X. Zeng, The microstructure and mechanical properties of deposited-in718 by selective laser melting, J. Alloys Compd. 513 (2012) 518–523.
- [52] J. Zuback, T. DebRoy, The hardness of additively manufactured alloys, Materials 11 (2018) 2070.
- [53] R. Reed, C. Rae, Physical metallurgy of the nickel-based superalloys, in: Physical Metallurgy (Fifth Edition), Elsevier, 2015, pp. 2215-2290.
- [54] R. Cozar, A. Pineau, Morphology of yand y precipitates and thermal stability of inconel 718 type alloys, Metall. Trans. 4 (1973) 47–59.
- [55] H. Xiao, S. Li, X. Han, J. Mazumder, L. Song, Laves phase control of inconel 718 alloy using quasi-continuous-wave laser additive manufacturing, Mater. Des. 122 (2017) 330–339.
- [56] E.L. Stevens, J. Toman, A.C. To, M. Chmielus, Variation of hardness, microstructure, and laves phase distribution in direct laser deposited alloy 718 cuboids, Mater. Des. 119 (2017) 188–198.